Mon. Not. R. Astron. Soc. **000**, 1–18 (2013) Printed 12 November 2013 (MN LATEX style file v2.2)

Characterizing diffused stellar light in simulated galaxy clusters

Weiguang Cui,[1,2⋆] G. Murante,[2] P. Monaco,[1,2] S. Borgani,[1,2,3] G.L. Granato,[2] M. Killedar,[1,2] G. De Lucia,[2] V. Presotto[2] and K. Dolag[4,5]

[1] *Astronomy Unit, Department of Physics, University of Trieste, via Tiepolo 11, I-34131 Trieste, Italy*
[2] *INAF, Astronomical Observatory of Trieste, via Tiepolo 11, I-34131 Trieste, Italy*
[3] *INFN –Sezione di Trieste, via Valerio 2, I-34100 Trieste, Italy*
[4] *University Observatory Munich, Scheinerstr. 1, D-81679 Munich, Germany*
[5] *Max-Planck-Institut fr Astrophysik, Karl-Schwarzschild Strasse 1, Garching bei Mnchen, Germany*

12 November 2013

ABSTRACT

In this paper, we carry out a detailed analysis of the performance of two different methods to identify the diffuse stellar light in cosmological hydrodynamical simulations of galaxy clusters. One method is based on a dynamical analysis of the stellar component, which separates the brightest central galaxy (BCG) from the stellar component not gravitationally bound to any galaxy, what we call 'diffuse stellar component' (DSC). The second method is closer to techniques commonly employed in observational studies. We generate mock images from simulations, and assume a standard surface brightness limit (SBL) to disentangle the BCG from the intra-cluster light (ICL). Both the dynamical method and the method based on the SBL criterion are applied to the same set of hydrodynamical simulations for a large sample of about 80 galaxy clusters. We analyse two sets of radiative simulations: a first set includes the effect of cooling, star formation, chemical enrichment and galactic outflows triggered by supernova feedback (CSF set); a second one also includes the effect of thermal feedback from active galactic nuclei triggered by gas accretion on to supermassive black holes (AGN set).

We find significant differences between the ICL and DSC fractions computed with the two corresponding methods, which amounts to about a factor of 2 for the AGN simulations, and a factor of 4 for the CSF set. We also find that the inclusion of AGN feedback boosts the DSC and ICL fractions by a factor of 1.5-2, respectively, while leaving the BCG+ICL and BCG+DSC mass fraction almost unchanged. The sum of the BCG and DSC mass stellar mass fraction is found to decrease from ~ 80 per cent in galaxy groups to ~ 60 per cent in rich clusters, thus in excess of that found from observational analysis.

We identify the average SBLs that yield the ICL fraction from the SBL method close to the DSC fraction from the dynamical method. These SBLs turn out to be brighter in the CSF than in the AGN simulations. This is consistent with the finding that AGN feedback makes BCGs to be less massive and with shallower density profiles than in the CSF simulations. The BCG stellar components, as identified by both methods, are slightly older and more metal-rich than the stars in the diffuse component. Relaxed clusters have somewhat higher stellar mass fractions in the diffuse component. The metallicity and age of both the BCG and diffuse components in relaxed clusters are also richer in metals and older.

Key words: galaxies: clusters: general — galaxies: evolution galaxies: formation — galaxies: statistics — galaxies: stellar content — cosmology: theory.

1 INTRODUCTION

The concept of intra-cluster light (ICL) was first introduced by Zwicky (1951), who pointed out the existence of stars be-

⋆ E-mail: wgcui@oats.inaf.it

tween galaxies within the Coma Cluster. However, the relevance of this baryonic component remained unclear until the advent of CCD photometry, that allowed accurate measurements in the Coma cluster to be carried out (Bernstein et al. 1995). Since then, several papers investigated the ICL in the Coma Cluster (Gregg & West 1998; Trentham & Mobasher 1998), in the Fornax Cluster (Theuns & Warren 1997), in the Virgo Cluster (Durrell et al. 2002; Feldmeier et al. 2004; Aguerri et al. 2005; Mihos et al. 2005; Rudick 2010), in other nearby clusters (Lin & Mohr 2004; Gonzalez et al. 2005; Krick & Bernstein 2007), and also at higher redshift (Zibetti et al. 2005; Toledo et al. 2011; Guennou et al. 2012; Burke et al. 2012).The ICL is now established to have low surface brightness with smooth distribution around the central galaxy, extending to large radii. However, the identification of this ICL in observations remains difficult and uncertain. Indeed, the typical surface brightness of the ICL is less than 1 per cent of the dark sky; also it can be contaminated by foreground and background galaxies; moreover, it is difficult (and somewhat arbitrary) to establish where the ICL begins and the associated brightest central galaxy (BCG) ends.

The kinematic information on the ICL can be obtained by discrete objects like planetary nebulae (PNe), which are excellent tracers for measuring the line-of-sight kinematics of intracluster stars (Arnaboldi & Gerhard 2010). With a suitable number of PNe, the mean radial velocities and velocity dispersions of the ICL can be determined. Such investigations have been carried out in a number of clusters (e.g. Ciardullo et al. 2005; Gerhard et al. 2007; Doherty et al. 2009; Arnaboldi et al. 2012)

On the theoretical side, in the last few years the analysis of simulated clusters provided an important contribution towards elucidating the nature and origin of the diffuse light component (e.g. Murante et al. 2004, 2007; Willman et al. 2004; Tutukov et al. 2007; Sommer-Larsen et al. 2005; Puchwein et al. 2010; Dolag et al. 2010; Rudick et al. 2006, 2009, 2011; Barai et al. 2009; Martel et al. 2012), which is now believed to contain valuable information on the dynamical history of the cluster and of the member galaxies. Diffuse light is also relevant for theoretical investigations of the evolution of the galaxy stellar mass function (Monaco et al. 2006; Yang et al. 2009) and of the stellar mass of satellite galaxies (Liu et al. 2010; Kang & van den Bosch 2008; Conroy et al. 2007). Generation of diffuse light associated to mergers, along the hierarchical assembling of cluster galaxies, has been introduced in recent semi-analytic galaxy formation models (Lo Faro et al. 2009; Guo et al. 2011; Somerville et al. 2008; Contini & et al. 2013). In theoretical studies, mostly based on simulations, the existence of an important component of stars that are not gravitationally bound to any galaxy, has been pointed out. While this dynamically distinct component is clearly related to, and often identified with, the observed ICL, it is not conceptually identical and cannot be directly compared with it. In the following, it will be dubbed as Diffuse Stellar Component (DSC). Clearly, it is of paramount importance to understand the relationship between the two. Careful analysis of simulations of clusters that model the formation of stars in galaxies is the most natural way to make progresses on this issue. This is the main aim of this paper.

A basic question about the ICL/DSC is what fraction of cluster stars are in these components. To date, consensus has not been reached yet on this issue either from observations or from simulations. This is attributable to some extent to the different adopted criteria to define and/or identify the ICL and the DSC. Observational estimates cover the range from 2 to 50 per cent. Lin & Mohr (2004) find a positive correlation of the ICL fraction with halo mass, reaching ~ 50 per cent for clusters of 10^{15} $M_{\odot}$. Zibetti et al. (2005) find that the ICL fraction is independent of cluster richness, with an average value of ~ 10 per cent. Krick & Bernstein (2007) note a large scatter in the ICL fraction from 6 to 20 per cent, but without any trend with mass. However, Sand et al. (2011) claim a declining stellar mass fraction as a function of halo mass, as reported also by Gonzalez et al. (2007). Similarly, theoretical studies have sometimes found no significant dependence of the ICL/DSC fraction on cluster mass (Dolag et al. 2010; Puchwein et al. 2010; Rudick et al. 2011; Contini & et al. 2013), while in other cases the ICL/DSC fraction has been found to increase with cluster mass (Purcell et al. 2007; Murante et al. 2007; Henriques et al. 2008; Martel et al. 2012; Watson et al. 2012). Contrasting claims have been made also on the dependence of the result on the identification method (Puchwein et al. 2010; Rudick et al. 2011).

In this paper we use and improve two methods to identify the DSC and the ICL, respectively, in simulations (Section 3). The dynamical method (dubbed SUBFIND from the name of the substructure identification algorithm; Springel et al. 2001; Dolag et al. 2009) is based on exploiting dynamical information available for star particles in simulations, so as to identify those particles belonging to the DSC. The SBL method (dubbed MAP algorithm) mimics typical observational procedures and is based on the generation of surface brightness maps, on which a threshold surface brightness criterion is imposed to identify the ICL. We apply these methods to two sets of radiative simulations of galaxy clusters and groups, based on including only the effect of galactic outflows triggered by supernova (SN) feedback and also adding the effect of thermal feedback from active galactic nuclei (AGN), respectively. The plan of the paper is as follows. We introduce the simulations in Section 2, while we describe in Section 3 the methods for the DSC/ICL identification. In Section 4 we present our results on the relationship between the ICL and the DSC identified with the two methods, and on the effect of the AGN feedback on these components. Our main results are summarized and discussed in Section 5.

2 THE SET OF SIMULATED GALAXY CLUSTERS

We summarize here the basic features of the set of simulated clusters analysed in this work. For more detailed information on the generation of initial conditions and basic properties of the simulated clusters, we refer the reader to Fabjan et al. (2011); Bonafede et al. (2011).

The simulations have been carried out with the TreePM-SPH GADGET-3 code, a more efficient version of GADGET-2 (Springel 2005), which includes a scheme of domain decomposition allowing an improved workload balance, especially in simulations, like those considered here, where

the computational cost is dominated by few prominent non-linear structures.

The clusters are extracted from high resolution re-simulations of 29 Lagrangian regions, taken from a large volume, low-resolution N-body cosmological simulation (see more details in Bonafede et al. 2011). The parent simulation follows 1024^3 DM particles within a periodic box of comoving size $1h^{-1}$Gpc, assuming a flat ΛCDM model: matter density parameter $\Omega_{\rm m} = 0.24$; baryon density parameter $\Omega_{\rm b} = 0.04$; Hubble constant $h = 0.72$; normalization of the power spectrum $\sigma_8 = 0.8$; primordial power spectral index $n_s = 0.96$. Each Lagrangian region has been re-simulated at higher resolution employing the *Zoomed Initial Conditions* (ZIC) technique (Tormen et al. 1997). Each high-resolution Lagrangian region is taken to be large enough so that no contaminant low-resolution particle is found at $z = 0$ within five virial radii of the central cluster. Given the resulting large size of the high-resolution regions, each of them contains more than one galaxy group or cluster not contaminated by low-resolution particles within the virial region. Gas particles are added only in the high-resolution regions, where DM and gas particles have masses of $8.47 \times 10^8\ h^{-1}\,{\rm M}_\odot$ and $1.53 \times 10^8\ h^{-1}\,{\rm M}_\odot$ respectively. The Plummer–equivalent gravitational softening is fixed to $5\,h^{-1}$kpc in comoving units below $z = 2$, while being fixed in physical units at higher redshift. The B-spline smoothing length for the SPH computations is allowed to reach a minimum value of half of the gravitational softening.

All the simulations analysed in this paper include radiative gas cooling, star formation and chemical enrichment. Radiative cooling rates are computed following the same procedure by Wiersma et al. (2009), by accounting for the contribution to cooling from 11 elements (H, He, C, N, O, Ne, Mg, Si, S, Ca, Fe), provided by the CLOUDY photoionization code (Ferland et al. 1998) for an optically thin gas in photoionization equilibrium, also accounting for the presence of the cosmic microwave background and of UV/X-ray background radiation from quasars and galaxies (Haardt & Madau 2001). Star formation is described through the sub-resolution model originally introduced by Springel & Hernquist (2003). In this model each gas particle exceeding a threshold density of $n_{\rm H} = 0.1{\rm cm}^{-3}$ is assumed to be multiphase and star forming, with a hot ionized phase coexisting in pressure equilibrium with a cold phase which describes the interstellar medium and provides the reservoir for star formation. In addition to the density criterion, we also introduce a threshold temperature of 2.5×10^5K, below which a gas particle can be treated as multiphase. Chemical enrichment is included by following the production of heavy elements from SN-II, SN-Ia and low- and intermediate- mass stars, as described by Tornatore et al. (2007). Stars of different mass, distributed according to a Chabrier IMF (Chabrier 2003), release metals over the timescale determined by their mass-dependent lifetimes, taken from Padovani & Matteucci (1993).

In this paper, we will focus on two sets of such cluster simulations. Besides the effect of radiative cooling and star formation, a first set contains cooling, star formation and the effect of kinetic feedback through galactic outflows triggered by SN-II explosions (CSF set hereafter). In the model of kinetic feedback, originally introduced by Springel & Hernquist (2003), a multi-phase star-forming gas particle is assigned a probability to be uploaded in galactic outflows, which is proportional to its star formation rate. We assume $v_w = 500\,{\rm km\,s}^{-1}$ for the outflow velocity and a mass-upload rate that is two times the value of the star formation rate of a given particle.

Besides kinetic feedback, a second set of simulations also include the effect of a thermal AGN feedback (AGN set hereafter). The model of this AGN feedback is largely inspired to the original implementation by Springel et al. (2005), but with some significant changes, as described in detail by Ragone-Figueroa et al. (2013). Super massive black holes are initially seeded as sink particles, with an initial mass of $5 \times 10^6\ h^{-1}\,{\rm M}_\odot$, within haloes identified by a friend-of-friend algorithm which have a minimum mass of $2.5 \times 10^{11}\ h^{-1}\,{\rm M}_\odot$ and do not already include a black hole particle. Super massive black holes grow in mass by merging with other black holes and via gas accretion that proceeds at an Eddington–limited Bondi rate. Differently from the original implementation by Springel et al. (2005), the black hole mass increase by gas accretion does not proceed through a stochastic swallowing of gas particles. Instead, the dynamical mass of a black hole particle continuously increases according to the accretion rate, without removing the surrounding gas. This prescription causes a minor violation of mass conservation. However, it improves the numerical stability of the accretion process and prevents accretion from affecting the gas distribution on scales that are physically implausible because of the limited numerical resolution (Ragone-Figueroa et al. 2013; see also Wurster & Thacker 2013). A radiative efficiency parameter, ϵ_r, describes the fraction of the accreted rest-mass energy that is radiated from the black hole, while a feedback efficiency parameter, ϵ_f, corresponds to the fraction of this radiated energy that is thermally coupled to the surrounding gas. We further assume that feedback enters in a quiescent radio mode whenever the accretion rate drops below one-hundredth of the Eddington limit. In this regime, feedback efficiency is increased by a factor of 4 (see also Sijacki et al. 2007; Fabjan et al. 2010). As shown in Ragone-Figueroa et al. (2013), our implementation of the AGN feedback allows us to reproduce the observed relation between black hole masses and stellar masses of host galaxies for the adopted values of $\epsilon_r = 0.2$ and $\epsilon_f = 0.2$.

3 THE DIFFUSE LIGHT IDENTIFICATION METHODS

In observations, two methods are usually employed to identify the ICL. The first one is to attribute to the ICL all the light coming from outside some optical boundaries of galaxies, usually defined by a fixed surface brightness limit (SBL) (e.g. Feldmeier et al. 2004; Mihos et al. 2005; Zibetti et al. 2005). The second method is to separate the BCG from ICL by modeling the surface brightness with two profiles (usually de Vaucouleurs or Srsic), after masking satellite galaxies and foreground contamination (e.g. Gonzalez et al. 2005; Seigar et al. 2007). In this paper, we apply the first method, after generating mock cluster images from the simulations, as described in Section 3.2 (see also Rudick et al. 2011). In simulations, it is possible to exploit the full dynamical information available to investigate the DSC (e.g. Murante et al. 2007; Rudick et al. 2011; Puchwein et al. 2010; Dolag et al.

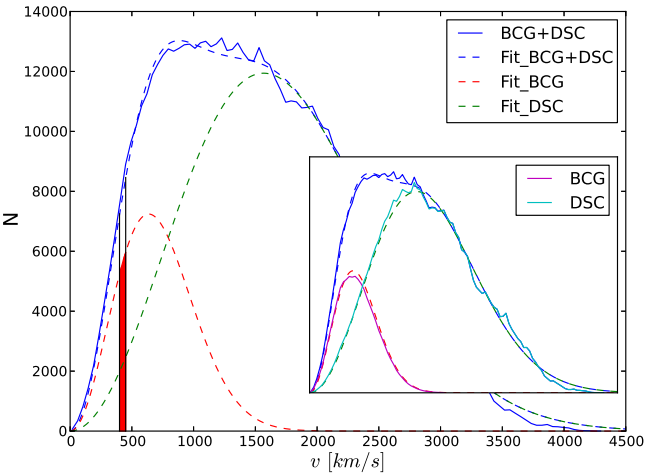

Figure 1. Velocity histograms of the BCG and DSC stellar particles (blue solid line) and the corresponding double Maxwellian fit (blue dashed line). The red and green dashed lines are the two single Maxwellian fitting profiles. The two vertical lines indicate a velocity bin, whose red area represents the stars assigned to the BCG with the criterion based on potential energy described in Section 3.1. The solid magenta and cyan lines in the small inset panel show the velocity histograms of the BCG and DSC stars after the separation process, along with the corresponding individual single-Maxwellian fitting curves.

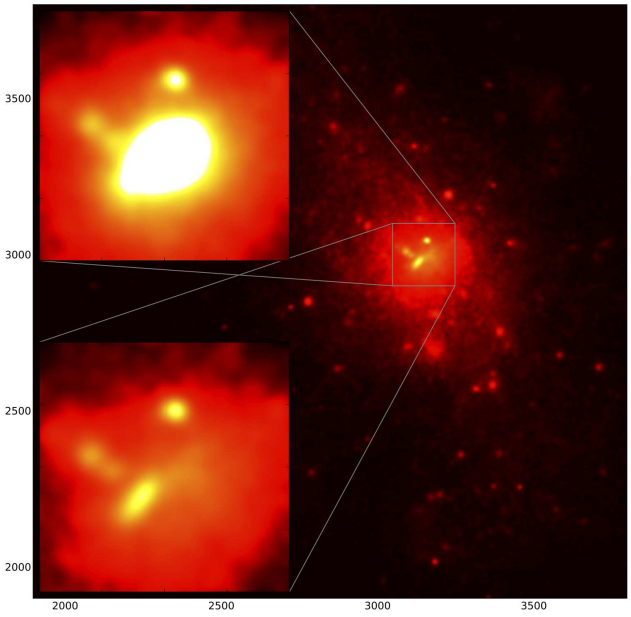

Figure 2. Projected density map of the DSC in one simulated cluster at $z = 0$. The lower and upper zoomed-in panels show the centre of the cluster without and with the BCG, respectively. Units of the axes are in h^{-1} kpc.

2010), which is defined by the stars gravitationally bound to the gravitational potential of a cluster but not to that of any galaxy (Dolag et al. 2010, e.g.). There are several algorithms that analyse the kinematics of star particles and separate the DSC from the BCG (Murante et al. 2004; Puchwein et al. 2010; Dolag et al. 2010, and references therein). In this paper, we use a slightly modified version of SUBFIND (Dolag et al. 2010), which we describe in detail in Section 3.1. We refer the first method as SBL method which applies an algorithm named MAP. While the second method is called dynamical method which uses the SUBFIND algorithm.

Although the ICL and the DSC are clearly related to each other, in general they do not include the same population of stars. Comparing their properties is quite interesting for a number of reasons, such as inferring the dynamical origin of the ICL, whose identification is based on observational criteria not related to the kinematics of stars.

3.1 The dynamical method

The SUBFIND algorithm (Springel et al. 2001; Dolag et al. 2009) algorithm was originally introduced to identify substructures within a group of particles identified by applying the friends-of-friends (FoF) algorithm. Afterwards, the SUBFIND algorithm was suitably modified to separate the DSC from the BCG by Dolag et al. (2010). SUBFIND identifies the main sub-halo as the most massive gravitationally bound substructure, which includes both the BCG and DSC. The velocity dispersion distribution of star particles inside this main sub-halo is best described by a double Maxwellian (see more details in Dolag et al. 2010; Puchwein et al. 2010). It is then natural to assign the lower velocity dispersion component to the BCG, while the higher velocity dispersion component is assumed to feel the general potential of the cluster and, as such, is identified with the DSC.

While this statistical procedure provides an estimate of the stellar mass fraction in the BCG and DSC components, it does not allow one to assign individual star particles to either one of the two components. On the other hand, this is required for most of the analysis presented in this paper, and is implemented by means of an iterative analysis (Dolag et al. 2010; Puchwein et al. 2010). In brief, a radius is iteratively searched, such that the velocity distribution of particles which are gravitationally bound to the matter contained within that radius; matches the lower dispersion Maxwellian component. Those star particles are defined to belong to the BCG.

Here, we also employ an analysis of binding energies, but with a novel algorithm that is both simpler and does not require iterations. Furthermore, this new algorithm can avoid mis-matching between the fitted velocity dispersion profiles and these from the simulated BCG particles and DSC particles. In each velocity bin, we assign to the BCG all the star particles whose potential is lower than a limiting value, defined so that the mass fraction below it matches the ratio between the area below the lower Maxwellian within a given velocity bin (red region in Fig. 1) and the area below the total velocity distribution encompassed by the same bin. The remaining particles are assigned to the DSC. In this procedure, the DSC and BCG are allowed to be spatially overlapping, as they do in the double Maxwellian fit. In this way the two components provide an exact fit to the two Maxwellian profiles, without the need of an iteration process which could suffer from convergence problems. Moreover, it

is physically reasonable to assign lower potential particles to the BCGs.

In order to give a visual impression of how this method separates the two components, we show in Fig. 2 the projected image of the DSC and BCG of the same simulated cluster. Colour coding is based on the projected surface density of star particles. Quite clearly, removing the BCG components provides a rather smooth distribution of the remaining diffuse component.

3.2 The SBL method

To generate surface brightness maps of the clusters, we follow the same procedure as in Cui et al. (2011). Each star particle of the FoF group is treated as a Simple Stellar Population (SSP) with age, metallicity and mass given by the corresponding particle's properties in the simulation, and adopting the same initial mass function (IMF) (a Chabrier IMF; Chabrier 2003). The spectral energy distribution (SED) of each particle is computed by interpolating the SSP templates of Bruzual & Charlot (2003). A standard Johnson V-band filter is applied to this SED to calculate its V-band luminosity. Then, we smooth to a 3D mesh grid both the luminosity and the mass of each star particle with the same spline kernel used for the SPH calculations. The mesh size is fixed to 5 h^{-1} kpc (corresponding to the gravitational softening length), and we use 64 SPH neighbours. The exact value of these parameters does not significantly affect our final results (see also Rudick et al. 2006). Finally, projecting this 3D mesh in one direction yields the 2D photometric image. Since only the star particles within the FoF group are used, we take out all the contamination from the background or foreground galaxies, that might significantly affect the observational results. We neglect dust reprocessing in this procedure, which should have less effect in the dust-free clusters. To measure the ICL in the mock images, we use the SBL usually adopted in observations $\mu_V > 26.5$ mag arcsec^2 (e.g. Mihos et al. 2005; Feldmeier et al. 2002; Rudick et al. 2011). The choice of a SBL of $\mu_V > 26.5$ for the SBL method is motivated by the fact that this surface brightness is used to define the Holmberg radius (Holmberg 1958), a commonly adopted method to define the isophotal size of galaxies. This SBL is also used to mark the transition where the ICL begins to take on a distinct morphology from the galactic light in both simulations (Rudick et al. 2006, 2009, 2011) and observations (Feldmeier et al. 2004; Mihos et al. 2005; Rudick et al. 2010). However, applying this simple SBL cut to clusters of various masses and dynamical states, may not be able to capture individual BCGs.

To understand the role of the SBL in the BCG/ICL separation, we also apply two other cuts, one magnitude brighter and fainter than the above reference value. To define the mass of the BCG, we draw circular annuli centred on the pixel containing the most bound particle with width $dR = 1.5$ pixel. We then define the outer boundary of the BCG as the innermost annulus in which the fractional area with surface brightness fainter than 26.5 mag arcsec^2 is greater than 0.5, and we attribute to BCGs the integrated flux of all the pixels (with $\mu_V < 26.5$ mag arcsec^2) inside this radius. Rudick et al. (2011) also applied a similar procedure to generate surface brightness maps of simulated clusters. However, their procedure is based on a dark matter only simulation.

4 RESULTS

4.1 The ICL-DSC fraction

As already discussed in Section 1, the fraction of the ICL and the DSC have been investigated in previous analyses, both in simulations and in observations, with results sometimes discordant. This can be partly attributed to the different methods and definitions adopted to identify these components. In the following, all the fractions of stars in one of these components are computed within r_{500}, which is defined as the radius within which the mean matter density is 500 times the critical cosmic density.

In the left panel of Fig. 3, we show the fraction of the total stellar mass in the DSC, as a function of halo mass M_{500}. We have used filled and open symbols to distinguish between relaxed and un-relaxed clusters, defined following the method of Killedar et al. (2012). This method consists in computing the offset between the minimum potential position and centre of mass, calculated within a range of radii $\zeta_i r_{vir}$, with ζ_i going from 0.05 to 2 in 30 logarithmic steps. A cluster is defined as relaxed if the offset is less than 10 per cent of $\zeta_i r_{vir}$ for all radii.

For the CSF set, the DSC mass fraction turns out to vary from $\sim$ 50 to 40 per cent when going from lower to higher halo mass, with fairly large scatters around these values. This fraction is $\sim$ 55 per cent for the AGN simulations, almost independent of the halo mass. The DSC fraction for the CSF set is consistent with that found byPuchwein et al. (2010), and slightly higher than that reported by Dolag et al. (2010). Furthermore, the DSC fraction is about 10 per cent higher for the AGN set, at variance with the claim of Puchwein et al. (2010) that this fraction does not significantly change with and without AGN feedback. Relaxed clusters tend to have higher DSC fractions than un-relaxed clusters. Relaxed clusters should be dynamical evolved systems, compared to the clusters under merging. Thus, a higher DSC fraction in relaxed clusters can be understood if the diffuse star particles mainly come from the satellite galaxies undergoing merging and tidal stripping. We checked that the DSC fractions within r_{200} have a very similar behaviour.

In the right panel of Fig. 3 we show the BCG+DSC mass fractions within r_{500}. With the inclusion of the BCG mass, these fractions boost to $\sim 60-80$ per cent for the CSF case, and to $\sim$ 80 per cent for the AGN case. Similarly to the DSC mass fraction in the left panel, the BCG+DSC fraction is higher for relaxed clusters than for un-relaxed ones.

The same cut at r_{500} is applied to the simulated clusters after computing the surface brightness maps. Then, a SBL is applied to the maps to identify the ICL, whose mass is defined as the stellar mass within those pixels that are brighter than the surface brightness limit. As discussed in Section 3.2, both luminosity and mass of star particles are smoothed in the same way, so that each pixel is assigned mass and luminosity consistently.

In Fig. 4, we show the ICL mass fraction from the SBL method. Upper left, upper right and lower left panels show

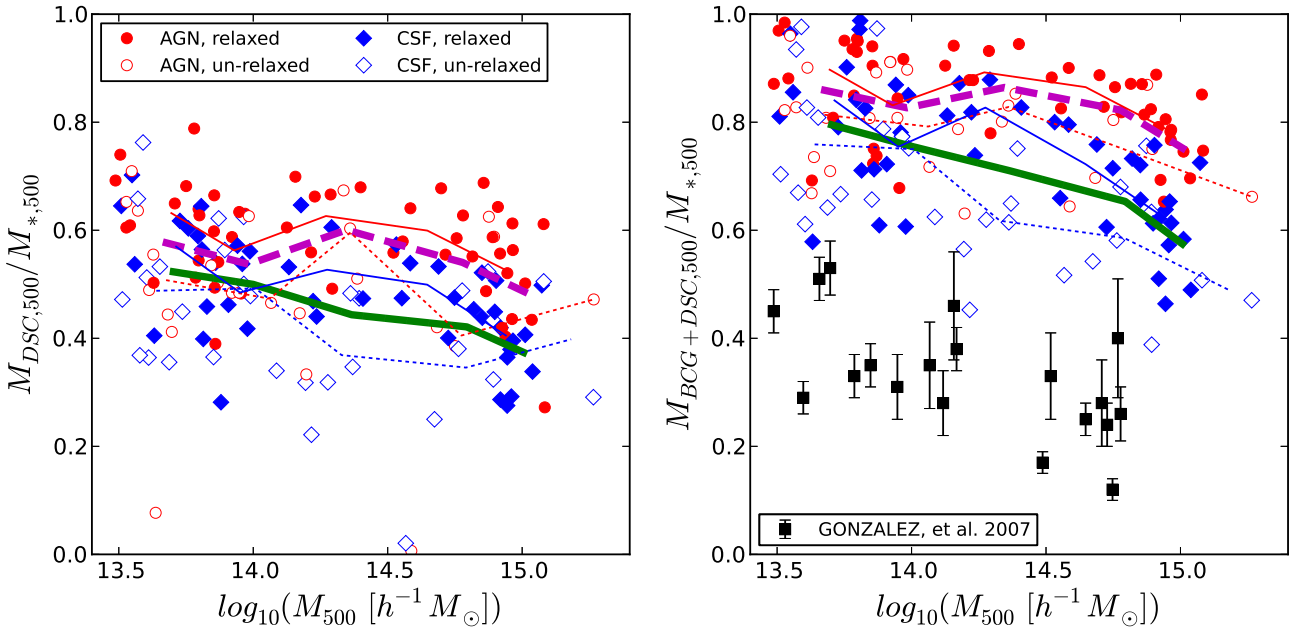

Figure 3. Left panel: The DSC fraction within r_{500}, computed with the dynamical method, as a function of halo mass M_{500}. Right panel: as in the left panel but for the BCG+DSC fraction. Blue squares and red circles represent the CSF and AGN simulations, respectively. The solid green and the dashed magenta thick lines are the corresponding averages. We have used filled and open symbols to denote relaxed and un-relaxed clusters. The thin solid and dotted lines are the averages for filled and open symbols, respectively.

the ICL mass fraction obtained using three different surface brightness limits: $\mu_V > 25.5, 26.5, 27.5$, respectively. The symbols and lines have the same meaning as in Fig. 3. Obviously, using a higher SBL, fewer pixels are selected as belonging to the ICL component, thus providing lower ICL mass fractions. This trend with the SBL is stronger for the AGN simulations; this reflects the fact that the galaxies in the AGN set are less concentrated than in the CSF set. The ICL fractions for the AGN set weakly decrease with halo mass, while the CSF clusters show no such trend. The decrease in the AGN set is in contrast with the increasing trend found in several observations, as reported in the Introduction. For the choice of $\mu_V > 26.5$, the ICL fraction is $\sim 30-20$ per cent for the AGN set, from low to high halo masses, and ~ 15 cent for the CSF set. Those values are in line with those found in simulations by Rudick et al. (2011) and by several authors from observational data (e.g. Zibetti et al. 2005; Krick & Bernstein 2007).

In the lower right panel of Fig. 4, we show the BCG+ICL mass fraction obtained with the SBL method using the reference value for the surface brightness limit. The mass of the BCG is computed as described in Section 3.2. The mass fractions in the BCG+ICL obtained with the SBL method agree well with the BCG+DSC fractions obtained with the dynamical method (see the right panel of Fig. 3) for both sets of simulations. This means the two methods only differ in the way they separate the diffuse and the BCG components. With $\mu_V = 26.5$, the SBL method assigns more star particles to the BCG than the dynamical method does.

With both simulations, we produce a higher BCG+DSC/ICL fraction than the observation results of Gonzalez et al. (2007) (see left panel of Fig. 3 and lower left panel of Fig. 4). This is a well known problem of numerical simulations, which is also found in similar analyses by Planelles et al. (2013) and Puchwein et al. (2010). A too large mass of BCGs in simulations may not fully explain the discrepancy. In fact, as shown in Figs 3 and 4, including AGN feedback in our simulations increases the mass fraction of BCG+ICL, despite the reduction of the BCG mass. A possible explanation for the too large stellar mass fraction in the BCG+DSC/ICL may lie in the limited numerical resolution of our simulations, which should produce too fragile galaxies that are easily disrupted within the cluster environment. On the other hand, we also point out that the conversion of galaxy luminosities to masses in observational data could also be affected by systematic uncertainties. In their analysis, Gonzalez et al. (2007) assumed a constant $M/L_I = 3.6$ to convert observed luminosities into stellar masses for the ICL and for the whole galaxy population. Recent works (e.g. Conroy & van Dokkum 2012; Conroy et al. 2013; Spiniello et al. 2013) show that the stellar IMF and, therefore, the resulting M/L value could depend on the velocity dispersion, i.e. the mass of the galaxy. In particular, M/L is shown to be a growing function of the galaxy mass. In this case, using a fixed mass-to-light ratio to convert luminosities in masses could lead to an under-estimate of the BCG mass with respect to the rest of the cluster galaxy population, and, thus, to an under-estimate of the stellar mass fraction in the BCG+ICL. This under-estimate will affect more significantly the most massive clusters rather than less massive ones, which are dominated by the BCG in their total cluster stellar mass. In order to provide a rough

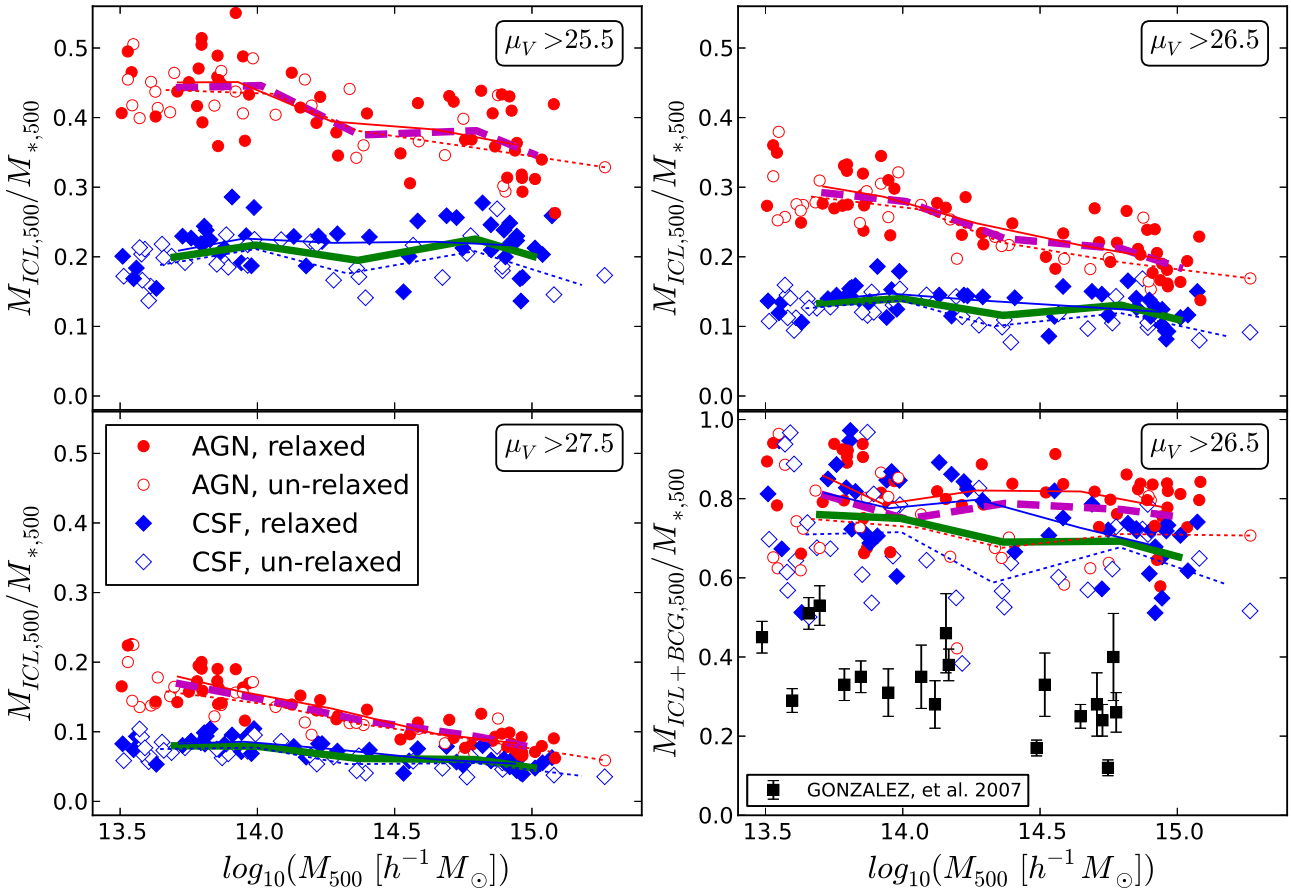

Figure 4. The ICL mass fraction within r_{500}, from the SBL method, as a function of halo mass M_{500} . The upper panels and the lower left panel show the ICL fractions computed assuming different values of the SBL, as indicated in each panel (in unit of mag arcsec^2). The symbols and lines have the same meanings as Fig. 3 for the relaxed and un-relaxed clusters. The lower right panel shows the BCG+ICL fraction with a SBL of $\mu_V > 26.5$mag arcsec^2.

estimate of the impact of such an effect, we assume BCGs to be characterized by the top-heavy IMF by Salpeter (1955), while the bulk of the cluster galaxy population following a Chabrier (2003) IMF. In the extreme case of most massive clusters, this effect can increase the BCG+ICL stellar mass fraction by a factor of up to ~ 1.6. Clearly, a more precise estimate of this effect would require a more detailed analysis, which is beyond the scope of this paper.

4.2 Comparing the two simulation sets and the two methods

It is clear from Figs 3 and 4 that the two simulation sets produce significantly different DSC/ICL mass fractions for both methods. To make a detailed comparison between the two simulation sets, we first match the two halo catalogues. Since each simulated Lagrangian region contains few clusters, a halo in a CSF simulation is matched to its counterpart in the AGN simulation when the distance of their centres is less than 200 h^{-1} kpc and their halo mass difference is within 50 per cent. In case there is no match we simply exclude the halo from comparison, while if we find more than one match we choose the nearest pair.

In the left panel of Fig. 5 we quantify, for each simulation set, the difference in the DSC and ICL fraction obtained with the two methods. We show in the figure the ratio between the DSC fraction within r_{500} obtained with the dynamical method and the ICL fraction obtained from the SBL method with $\mu_V > 26.5$. The difference between the results obtained using the two methods is smaller for the AGN simulations, but even in this case the dynamical-motivated DSC fraction is higher by a factor of 2 than the SBL-based ICL, and the difference increases weakly with halo mass. Within the CSF simulations the difference between the two methods rises to a factor of $\sim 3-4$. In Rudick et al. (2011) it is reported that different methods can change the ICL fraction up to a factor of 2. This is consistent with our results with AGN feedback, while we obtain an even higher difference with the CSF simulations.

In the right panel of Fig. 5 we show, for each method, the ratio of the DSC or ICL fractions between the two simulation sets, as a function of M_{500} measured in the AGN set. For both methods AGN simulations give higher fractions than CSF simulations, by a factor of ~ 1.3 for the dynamical method and by ~ 2 for the SBL method. The fraction

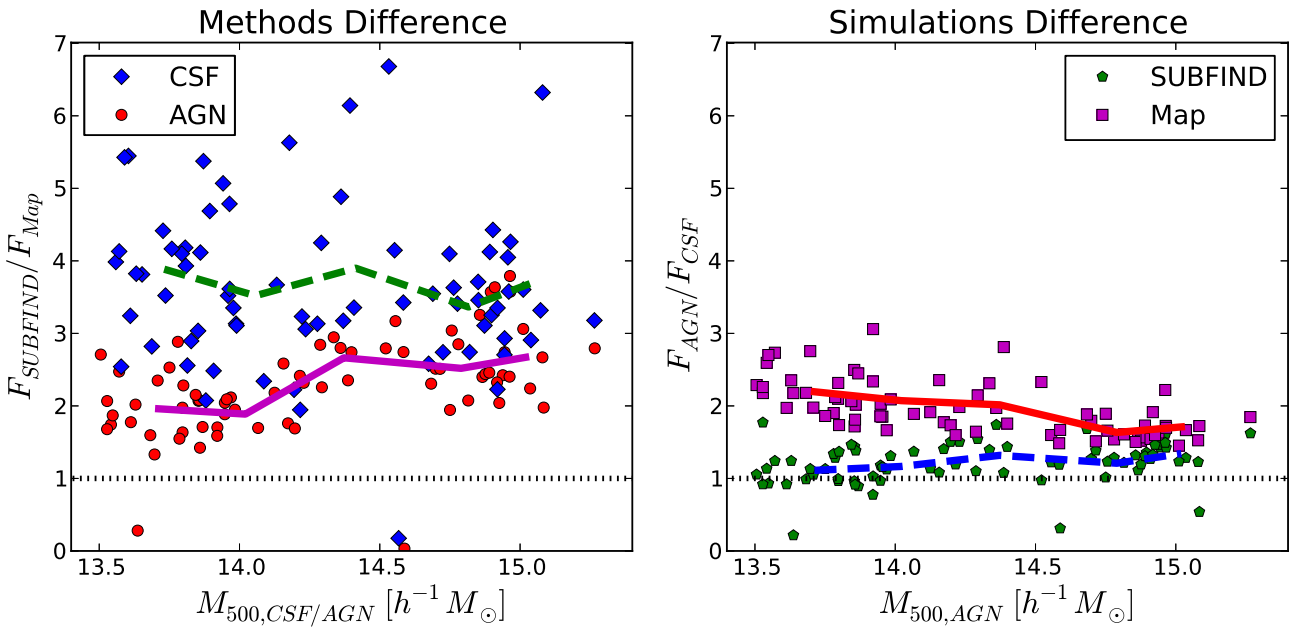

Figure 5. Left panel: the ratio between the DSC and ICL fractions obtained with the two methods as a function of M_{500}. The blue solid squares denote the CSF simulations, while the red solid circles denote the AGN simulations. The dashed green and solid magenta lines show the mean value of blue squares and red circles, respectively. Right panel: ratio of the DSC/ICL fractions between the AGN and the CSF simulations, as a function of halo mass $M_{500,AGN}$ (we use the mass found in the AGN set). Magenta squares and red solid line refer to the ICL obtained with the SBL method; green pentagons and blue dashed line are for the DSC obtained with the dynamical method.

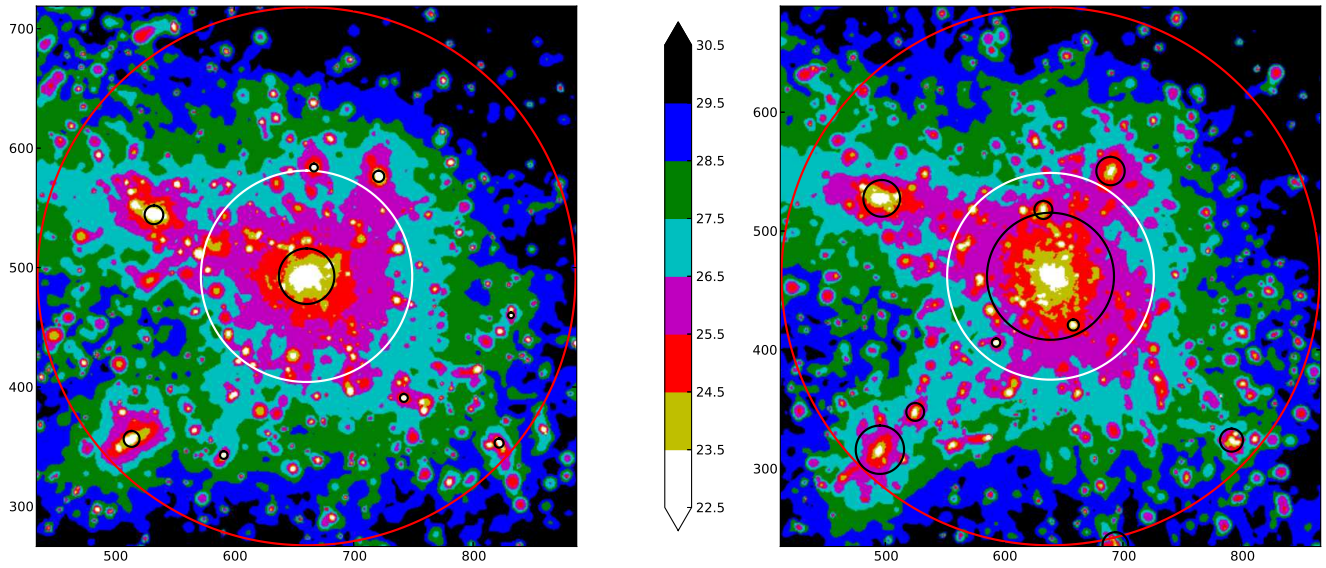

Figure 6. Projected surface brightness maps for one cluster with $M_{500} \approx 8 \times 10^{14}/M_\odot h^{-1}$ in the two simulation sets. The left panel shows the CSF simulation, while the right panel shows the corresponding AGN simulation. Colour levels follow apparent magnitude per square arcsec, as specified in the colour side-bar. The standard $\mu_V = 26.5$ surface brightness level corresponds to the level separating the cyan and magenta regions. The black circles show the radii of the BCG (the central one) and of satellite galaxies provided by SUBFIND. The red circle marks r_{500}. The smaller white circle shows the radius of the BCG as computed with MAP (Section 3.2).

from the dynamical method is less affected by the inclusion of AGN feedback than the fraction from SBL method.

To understand the origin of these differences, we first check the radii of the BCG as found with the SUBFIND and MAP algorithms. In Fig. 6, we show the surface brightness map (in rest-frame V-band apparent magnitude per $arcsec^2$) of one specific cluster with $M_{500} \approx 8 \times 10^{14} h^{-1} M_{\odot}$. The left panel gives the map for the CSF simulation, while the right panel is for the AGN one. Colour coding follows the curves of equal surface brightness given by the colour bar. We over-plot circles corresponding to r_{500} (red circle), to the radii of the BCG and of other satellite galaxies from SUBFIND (black circles) and to the BCG radius estimated with MAP (white circle). As for SUBFIND, circles have a radius equal to twice the half-mass radius of the stars that are assigned to that galaxy. As for MAP, we use a surface brightness limit of $\mu_V = 26.5$ and the procedure introduced in Section 3.2 (the largest radius for which more than half the pixels overtake the SBL). Clearly the sizes of the two BCGs differs significantly, especially in the CSF case (left panel of Fig. 6). The difference is smaller for the AGN case, but it still amounts to about a factor of 2. These trends neatly reflect the varying discrepancy of the DSC and the ICL in the CSF and AGN simulations, as seen in Fig. 5. The small black circles in Fig. 6 show the satellite galaxies' size from SUBFIND, which is also twice the half-mass radius. The sizes of satellite galaxies in the AGN case also agree better between the two methods.

4.3 The inferred surface brightness limit from the Dynamical Method

The connection between galaxy size, both the DSC and ICL can be further illustrated as follows. We plot in Fig. 7 the radial profile of surface brightness of the same cluster of Fig. 6 for all stellar particles (black lines) and for stars assigned by the dynamical method to the BCG (red lines) and to the DSC (blue lines). AGN feedback, as implemented in these simulations, has a strong effect on the BCG (see Ragone-Figueroa et al. 2013, for a detailed analysis), decreasing not only its final stellar mass but also its compactness. Based on Fig. 7, we argue that the surface brightness at which the profiles of the BCG and DSC cross identifies a suitable value of the surface brightness limit to be used in the MAP algorithm to best reproduce results of the dynamical method. Then, for each of our simulated clusters we construct the ICL and BCG surface brightness profiles and compute the value of surface brightness corresponding to their crossing. These crossing values are shown in Fig. 8 for all the clusters in both simulation sets; thick solid lines give mass-dependent averages, dashed lines show the average value for all clusters with $\log(M_{500}/\mathrm{h}^{-1}\mathrm{M}_{\odot}) > 13.5$. Crossing values of μ_V display a large scatter but are typically much brighter than $\mu_V = 26.5$, the value commonly used in observations to separate the BCG and ICL components. For the CSF simulations, the μ_V crossing values are rather bright, with an average of $\mu_V = 23$ and a tendency to be fainter for more massive clusters. For the AGN simulations their value is $\mu_V \simeq 24.75$ and show no trend with the cluster mass. This can be understood as an effect of AGN feedback that makes BCGs more extended and larger in size (Fig. 6), while lowering their total stellar mass (see also Ragone-Figueroa et al. 2013).

We then use the above average crossing values, $\mu_V = 23.00$ and $\mu_V = 24.75$ for the CSF and AGN cases, in the MAP algorithm to separate out the ICL from the BCG. This leads to an increase in the ICL fraction that becomes, as expected, similar to the corresponding DSC fraction. In the left-hand panel of Fig. 9 we show, as in Fig. 5, the ratio between the DSC and ICL fractions for the two sets of simulations. For comparison, average values from Fig. 5 are reported as dashed lines. Using the crossing values of the SBL, the difference between two methods decreases dramatically for both simulation sets, with average values raising only for small clusters in the CSF set, for which a constant crossing value of the surface brightness limit is clearly a poor fit (Fig. 8). Even the scatter is modest, most fractions differ by less than a factor of 2 from the average values. The right panel shows the ratio between the ICL fractions for two simulation sets, the thin red line giving the value found for a SBL of $\mu_V = 26.5$. The difference between the two simulation sets is now lowered by adopting the two new SBL values. The difference in these ICL fractions between relaxed and un-relaxed clusters is similar to earlier results.

This consistency check demonstrates that we understand the origin of the different results provided by the two methods for the two simulation sets. However, the dependence of the crossing value of SBLs upon physics tells us that fainter surface brightness crossings which have a better agreement with observations, are derived when AGN feedback is included. This indicates that these simulations with AGN feedback are headed in the right direction. The large scatter in both simulations suggests that also in observations, a single SBL applied to all BCGs could be too simplistic. We do not go as far as suggesting that a SBL, say, of $\mu_V = 24.75$ mag arcsec^{-2} should be used in observations to best reproduce the results of a dynamically motivated algorithm to identify the DSC. However, in the future, it could be possible to apply this method to infer the amount of the DSC once simulations are able to give convergent and realistic properties (both masses and sizes) of BCGs.

4.4 Velocity dispersions from the BCG and DSC

Since the DSC is the dynamical result of cluster evolution and is naturally separated from the BCG using velocity information provided by SUBFIND, it is interesting to investigate its velocity dispersion σ_{DSC}, as well as σ_{BCG}.

From the observational side, there are very few cases in which kinematic information on the ICL is available. Melnick et al. (2012) investigated the dynamical information of the ICL in RXJ0054.0-2823, an X-ray identified cluster at $z = 0.29$. They found that its BCG has a velocity dispersion of $\sigma \approx 150\,\mathrm{km\,s^{-1}}$, while the ICL velocity dispersion is $\sim 408\,\mathrm{km\,s^{-1}}$. They also found a steep increase in the velocity dispersion with radius qualitatively similar to what is observed by Coccato et al. (2011) in Hydra-I. This supports that the double Maxwellian velocity profile fitting method is a natural way of separating the two components (see also Toledo et al. 2011).

In Fig. 10, we present the velocity dispersions of BCGs and DSC from SUBFIND as a function of M_{200}. Those σ for both the BCG and DSC are consistent with the find-

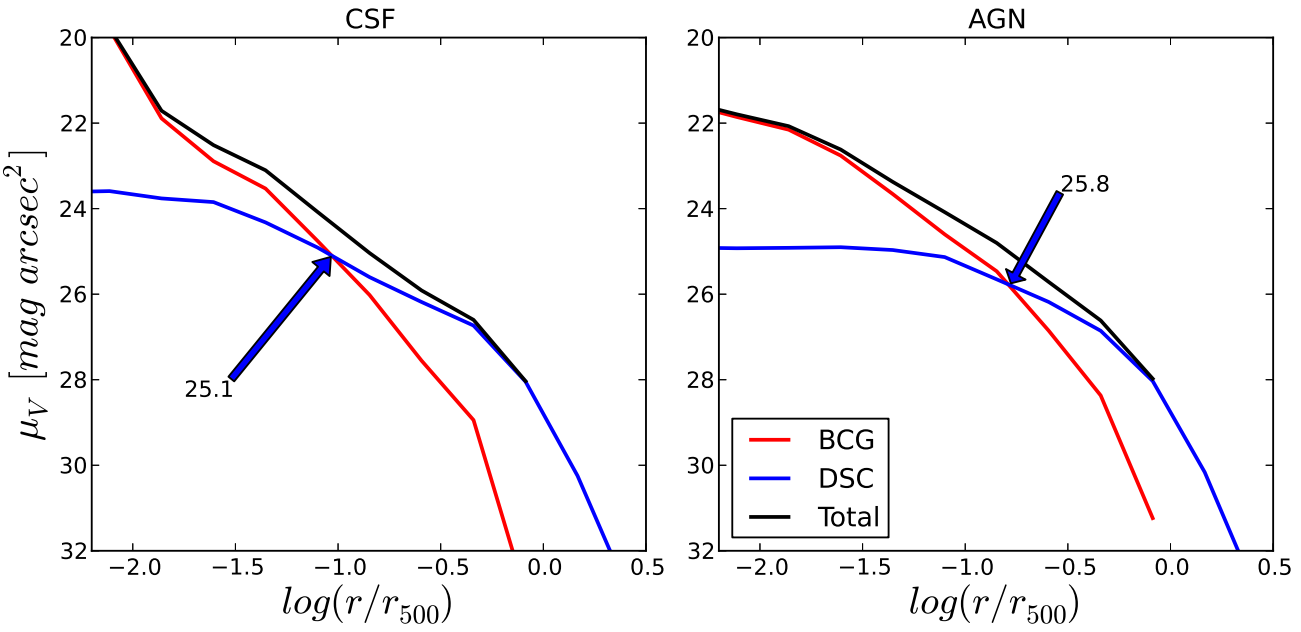

Figure 7. Surface brightness profiles contributed by the stars assigned to the BCG (red lines) and to the DSC (blue lines) by the dynamical method from the same cluster as Fig. 6. Black lines give the total surface brightness profile. Arrows highlight the points where the BCG and DSC curves cross. Left and right panels show the CSF and AGN simulations, respectively.

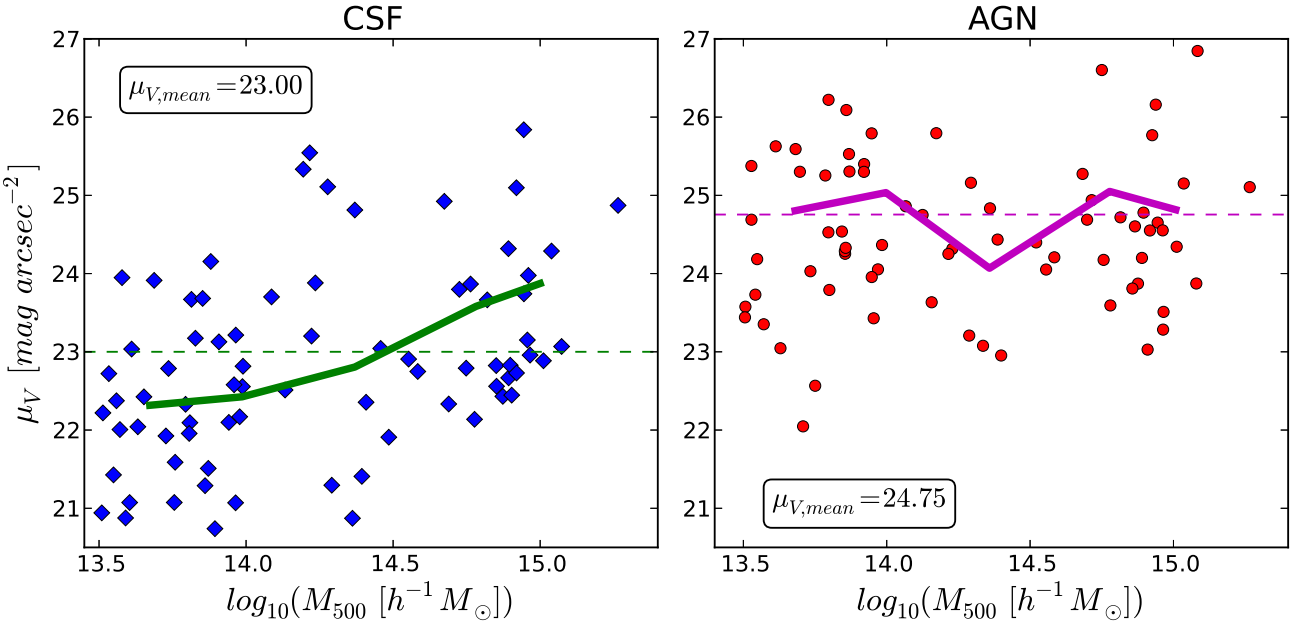

Figure 8. Surface brightness values for all clusters at the point where the surface brightness curves of the BCG and DSC cross, as a function of M_{500}. The left panel is for the CSF simulations, and the right panel is for the AGN simulations. The solid thick lines in the two panels give average value in mass bins, while the horizontal thin dashed lines mark averages for all clusters with $M_{500} \geqslant 13.5$.

ing in Dolag et al. (2010). Assuming a power-law of the form $\sigma \propto M^{\alpha}$, both components show a good fit with $\alpha \sim 0.36$ (except the BCG in the CSF set). This value of α for the AGN simulations is very similar to that found by Munari et al. (2013) from the analysis of these same simulation sets, in which galaxies and subhaloes are used as tracers. Un-relaxed clusters are under dynamic evolution, which results in a higher σ for both the BCG and DSC. That is why open symbols lie on the upper envelope of the mean. By definition the DSC stars should be freely floating in the

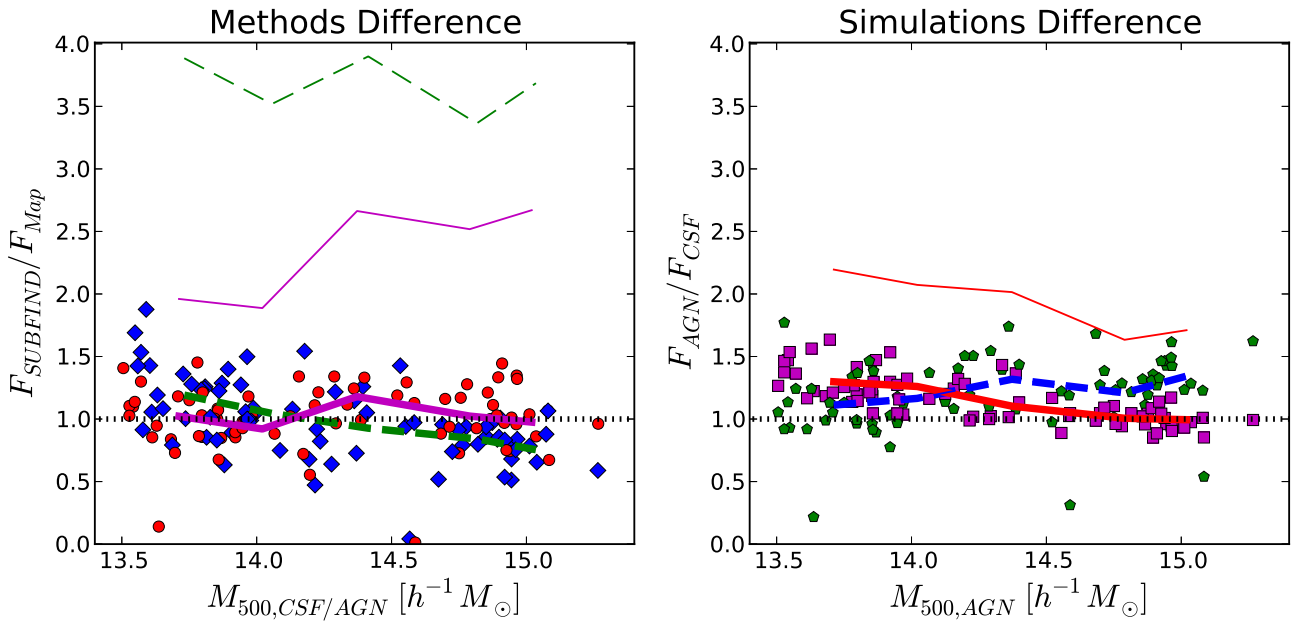

Figure 9. As in Fig. 5, we show, as a function of M_{500}, the ratio between the DSC and ICL fractions obtained with the two methods (left panel), and the ratio of the DSC/ICL fractions between the AGN and CSF set (right panel). In this case, the ICL fractions are obtained in MAP using SBLs of $\mu_V = 23.00$ and $\mu_V = 24.75$, as in Fig. 8, for the CSF and AGN set respectively. For an easier comparison with Fig. 5, we show results obtained with the standard 26.5 SBL as thin, green, dashed (CSF) and thin, solid, magenta (AGN) lines in the left panel, and as thin, red, solid line (SBL method) in the right panel.

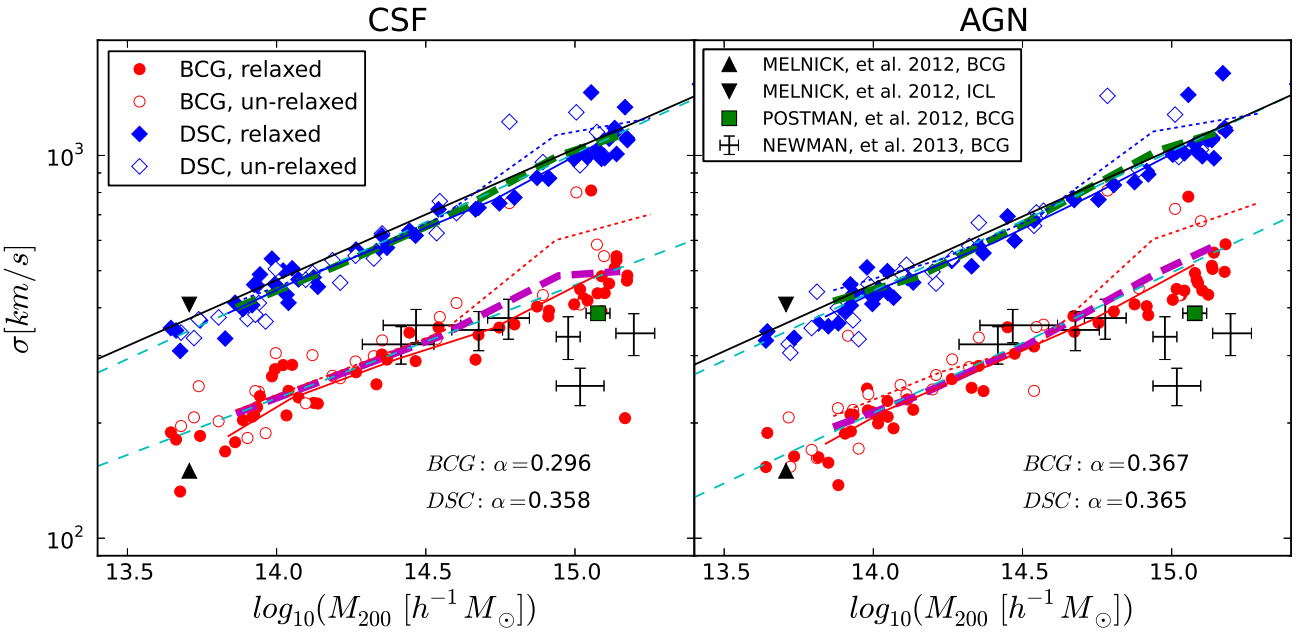

Figure 10. Velocity dispersions of BCGs and DSC as a function of halo mass M_{200}. Red circles and blue squares indicate BCGs and DSC, respectively. Thick dashed magenta and green lines show the corresponding binned mean values. Filled and open symbols denote relaxed and un-relaxed clusters, with the mean value showed by solid and dotted lines of the same colour. The two dashed cyan lines are the linear fitting results, with their slopes α reported in the lower right side of each panel. The black line shows the halo velocity dispersion fitting. Black triangles, filled green square and crosses with errorbars report observational results, according to the legend shown in the right panel.

gravitational potential of the cluster, and therefore should essentially have a velocity dispersion similar to that of the cluster as a whole (see the black fitting line). The velocity dispersion of the DSC is higher than that of the BCG in the same halo, as expected. The ratio is about a factor of 2 independent of halo mass. The values of velocity dispersion of the BCG and ICL found by Melnick et al. (2012) are in good agreement with our results (see the point-up and point-down black triangles in Fig. 10), thus demonstrating that our simulation captures the dynamical processes which lead to the formation of the ICL and to the dynamical diversity of the diffuse component with respect to the BCG component. The BCG velocity dispersion from Newman et al. (2013) and Postman et al. (2012) also shows a good match to our results. Note that we use a mean of the BCG velocity dispersion quoted from table 6 of Newman et al. (2013) with errors from last radius bin.

4.5 Physical properties of the BCG and ICL/DSC

In this section, we analyse the difference between luminosity and mass fractions associated with the ICL. Then, we focus on stellar metallicities and ages of the BCG and of the ICL/DSC components identified with the SUBFIND and MAP algorithms.

Observations provide estimates of the luminosity fraction of the ICL, while the fractions studied before are all in mass. Therefore a proper comparison with observational results requires to quantify the difference between luminosity and mass fraction in the ICL. This is conveniently done using the SBL method. In Fig. 11, we show the ratio of the two ICL fractions defined above for the two simulations sets (left: CSF; right:AGN). For the CSF simulations, the ratio of luminosity to mass fractions increases with halo mass, from ~ 0.9 to ~ 1.1, while the same quantity decreases for the AGN set from ~ 1.1 to ~ 1.

For the MAP algorithm, we adopt the reference value for the SBL, $\mu_V = 26.5$, to define the ICL, while the BCG is defined with the aperture method described in Section 3.2. All ages and metallicities are mass-weighted averages, which is different from luminosity-weighted observation results. In this section we show results for the AGN clusters only for the sake of brevity. Results for the CSF simulations are qualitatively similar with the difference that, due to the lack of quenching of late cooling flows, BCGs show unrealistically high metallicities, young ages and blue colours.

In Figs 12 and 14, we show mass-weighted metallicities and ages of star particles assigned to the BCG and to the DSC/ICL for both methods. In the upper panels we report the BCG and DSC/ICL metallicities or ages from dynamical (left) and SBL (right) methods. The BCG metallicities (Fig. 12) are roughly solar and show a weak increasing trend with halo mass. The DSC/ICL metallicities have a similar trend but with a systematic lower value. The dynamical method gives higher metallicities by 0.1 dex than the SBL method in both components. Ages (Fig. 14) decrease with halo masses for both BCGs and DSC/ICL. BCGs systematically have older age (~ 0.6 Gyr) than the DSC/ICL. Using mean age, Dolag et al. (2010) also found that BCGs are older (~ 0.8 Gyr) than the DSC. However, since the simulations analysed by Dolag et al. did not include AGN feedback, their ages for both components are about 4 Gyr younger than ours. Relaxed clusters show slightly higher metallicity and older age in both the BCG and the DSC/ICL components, for both methods.

In the lower panels of the same figures, we show the ratios of metallicities and ages of the BCG and the DSC/ICL components. In both cases, the metallicity in the BCG component is about 60 per cent higher than the DSC/ICL metallicity, and the age is ~ 6 per cent higher. The difference between relaxed and un-relaxed clusters is negligible in both metallicity and age ratios.

In Figs 13 and 15 we report stacked metallicity and age profiles of the BCG and DSC from the dynamical method obtained as follows. The cluster sample is divided into three sub-samples according to their M_{500} mass (see the labels above the three panels). For each sub-sample we distribute star particles in 10 logarithmically equispaced bins of r/r_{500}, ranging from -2.5 to 0, and for each bin we perform a mass-weighted average of metallicities or ages of all star particles in that bin.

Metallicity profiles of the BCG stars (Fig. 13) are higher and flatter in the central regions, dominated by the BCG itself, while there is a decreasing trend for the DSC stars. In the outer regions, dominated by the DSC, the declining trend has a similar slope for both the BCG and the DSC. Over all regions, the BCG metallicity profiles are higher than the DSC profiles by ~ 0.1 dex. Metallicity profiles for both the BCG stars and the DSC stars are clearly higher in the higher mass bins. On the contrary, age profiles for BCGs (Fig. 15) are contributed by a much older population of stars towards the centre, while the DSC age profiles are flatter, with only a slightly increasing trend in age in the inner region. The low halo mass bin shows steeper age profiles of those DSC stars compared to the other two mass bins.

Williams et al. (2007) found that intracluster population of stars in the field of the Virgo cluster is dominated by low-metallicity stars with $[M/H] \lesssim -1$, although this field appears to contain stars of the full range of metallicities probed $-2.3 \leqslant [M/H] \geqslant 0.0$, and with ages $\gtrsim 10$ Gyr. A similar result was obtained by Coccato et al. (2011) in the Hydra-I (A1060) cluster using long slit spectroscopy Lick indices. However, Melnick et al. (2012) claim that they found the ICL in their cluster to be dominated by old metal-rich stars. Using semi-analytical models, Contini & et al. (2013) found the ICL metallicity $log(Z/Z_{\odot}) \sim -0.2$, which agrees with our results. However, their BCG metallicity is about 0.1 dex poorer than ours. De Lucia & Borgani (2012) also showed that the stellar metallicities of the most massive galaxies would be too low with respect to observational data. The BCG metallicity in our simulations with AGN feedback is higher and closer to observations compared to the predictions from the semi-analytical models by De Lucia & Borgani (2012). The mean DSC/ICL age from our AGN simulations is ~ 9 Gyr, which is also comparable with observations. From the metallicity and age profiles of the DSC stars, we predict that the DSC in the inner cluster regions is mainly contributed by massive galaxies, which are old and metal rich; meanwhile, further out, they are slightly younger and more metal poor, which suggests stripping from dwarf galaxies, or perhaps from the outer regions of spiral galaxies.

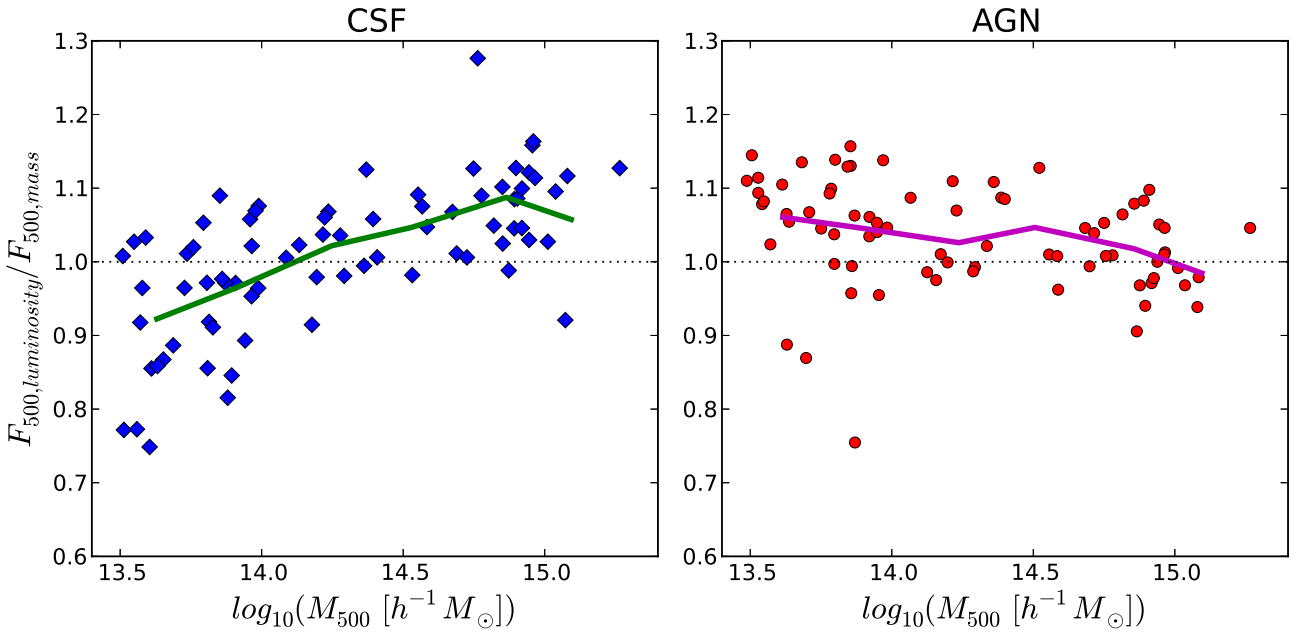

Figure 11. Ratio of the luminosity-weighted and mass-weighted ICL fractions obtained from the MAP algorithm, using the same SBL $\mu_V = 26.5$. The solid green and magenta lines are the average of the blue squares and red circles symbols in mass bins, respectively. Left and right panels show results for the CSF and AGN simulations, respectively.

5 DISCUSSION AND CONCLUSIONS

In this paper, we analysed hydrodynamic simulations of galaxy clusters and groups, with the aim of characterizing the diffuse component in the distribution of stars, and the corresponding properties of the intra-cluster light. This analysis has been carried out by applying two methods for the identification of such diffuse intra-cluster component. The first dynamical method is based on identifying stars belonging to the main substructure with the SUBFIND (Springel et al. 2001) algorithm for the identification of substructures. Besides separating the contribution of satellite galaxies, our implementation of SUBFIND (Dolag et al. 2010) also includes a prescription for separating the BCG from the diffuse stellar component by fitting the velocity dispersion profile with a double Maxwellian distribution. The second, observationally-oriented method is based on generating synthetic maps of V-band luminosity, applying a photometric synthesis code (Bruzual & Charlot 2003) to the distribution of star particles. The intra-cluster light was then separated from the light of the BCG by applying a surface brightness limit (SBL) cut to the map (see Section 3.2). These two methods have been applied to two sets of simulations; a first one including only the effects of cooling, star formation, chemical enrichment and galactic outflows driven by SN-II feedback (CSF set); and a second one by also including gas accretion on to supermassive black holes and the ensuing effect of thermal AGN feedback (AGN set).

The main results of our analysis can be summarized as follows.

- The DSC mass fraction within r_{500}, obtained with the dynamical method, amounts to $\sim 40-50$ per cent for the CSF simulations, slightly increasing to ~ 55 per cent for the AGN case. Those value are higher than the corresponding ICL mass fraction obtained with the SBL method when a value of $\mu_V = 26.5$mag arcsec^2 is used for the surface brightness limit separating the two components: ~ 15 per cent for the CSF simulations and $\sim 20-30$ per cent for the AGN simulations. Moreover, the DSC/ICL fractions in the AGN set is higher than that of the CSF set by a factor of $\sim$1.5 and $\sim$2 when using the dynamical and the SBL methods, respectively. Conversely, the BCG+DSC/ICL mass fractions within r_{500} are similar for the two methods, in both CSF and AGN simulations.

- A comparison with available observational results shows too large a stellar mass fraction in the BCG+ICL found in our simulations. This discrepancy may be contributed both by the limited numerical resolution that makes simulated galaxies too fragile in the cluster environment, and by a possible underestimate in observations due to the assumption of a constant M/L for the whole cluster galaxy population.

- To understand the differences in the DSC/ICL fractions obtained with the two methods, we investigate the projection effects. We verified that the size of the region in the surface brightness map to be identified with the BCG is significantly larger than the size of the BCG identified by the dynamical method. This explains the larger amount of mass in the ICL from the SBL method, with respect to that in the DSC from the dynamical method.

- For each cluster, we computed the value of the surface brightness threshold that gives the same ICL mass fraction as the DSC one provided by SUBFIND. These values are $\mu_V \simeq 23$ and 24.75 for the CSF and AGN simulations, respectively, thus much brighter than the values commonly adopted in observational studies, although with

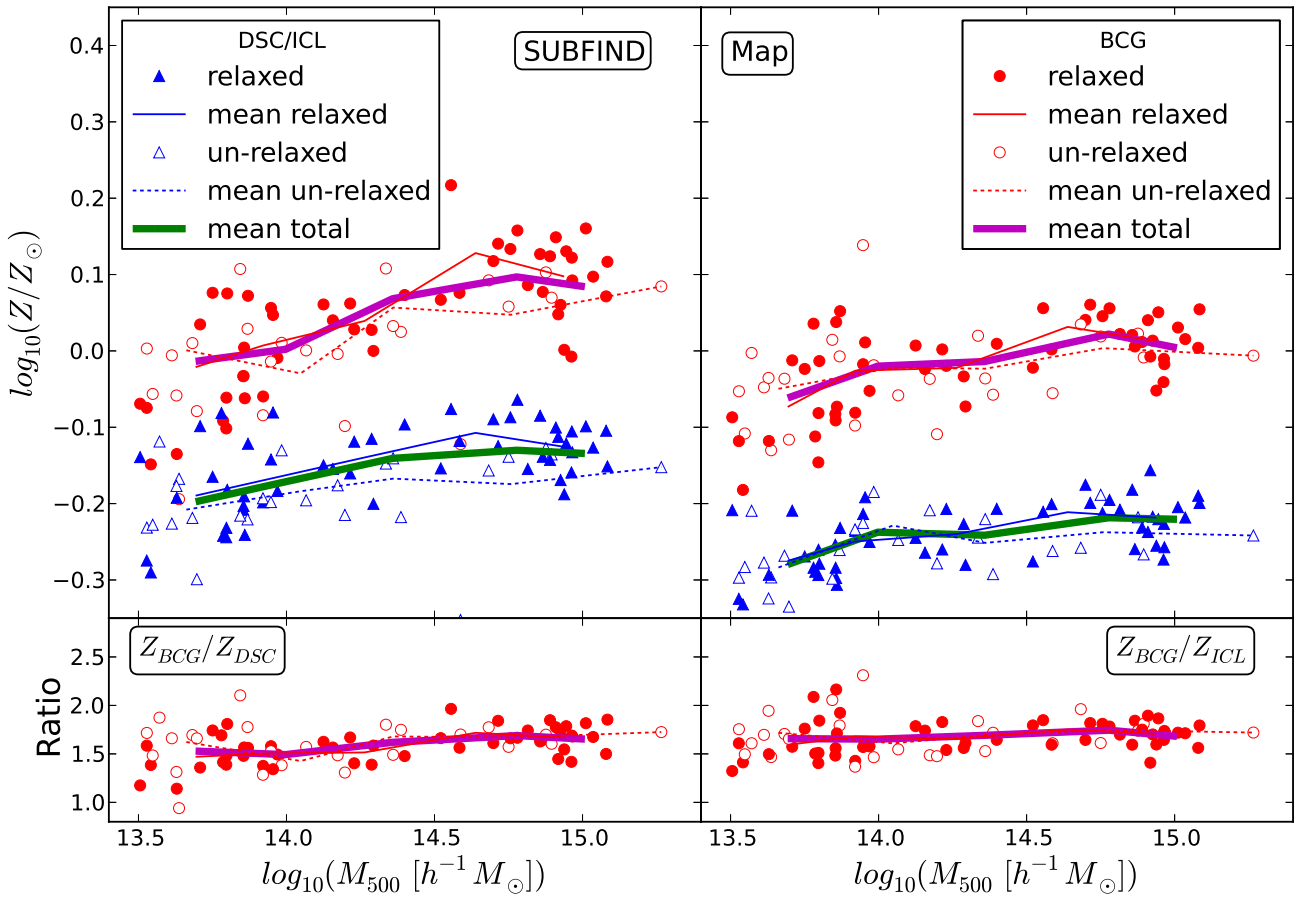

Figure 12. Upper panels: average, mass-weighted metallicity of BCGs and DSC/ICL (left: SUBFIND; right: MAP). Lower panels: ratios of metallicities of BCGs and DSC/ICL. Filled and open symbols denote relaxed and unrelaxed clusters, respectively. Thick magenta and green lines give the corresponding averages in mass bins, thin red and blue continuous and dotted lines give averages for relaxed and un-relaxed clusters for BCGs and DSC/ICL, respectively.

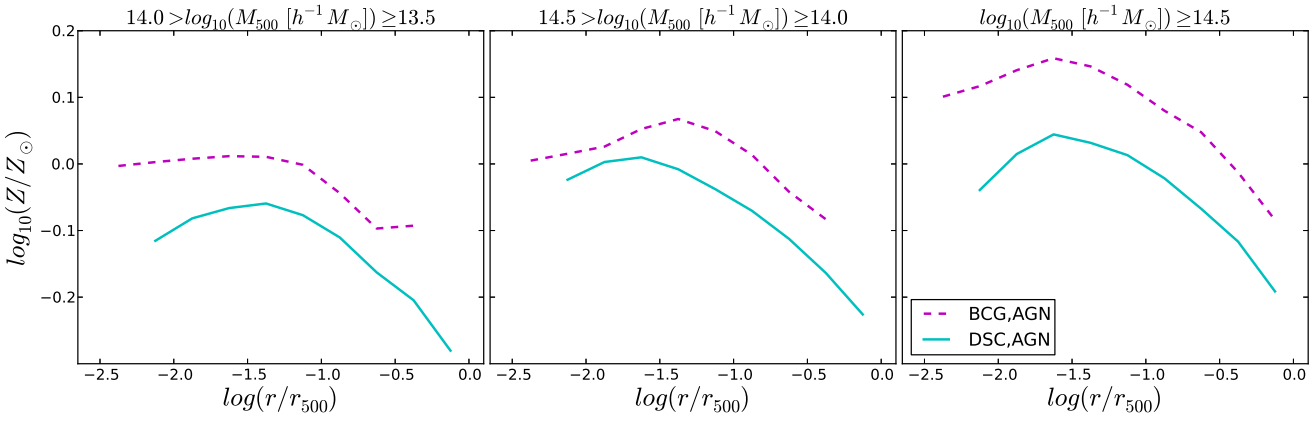

Figure 13. Average metallicity profiles of the BCG (purple dashed line) and DSC (solid cyan line) stars from the dynamical method, as a function of radius (normalized to r_{500}), for clusters belonging to three mass-limited subsamples, as reported in the label above the panels.

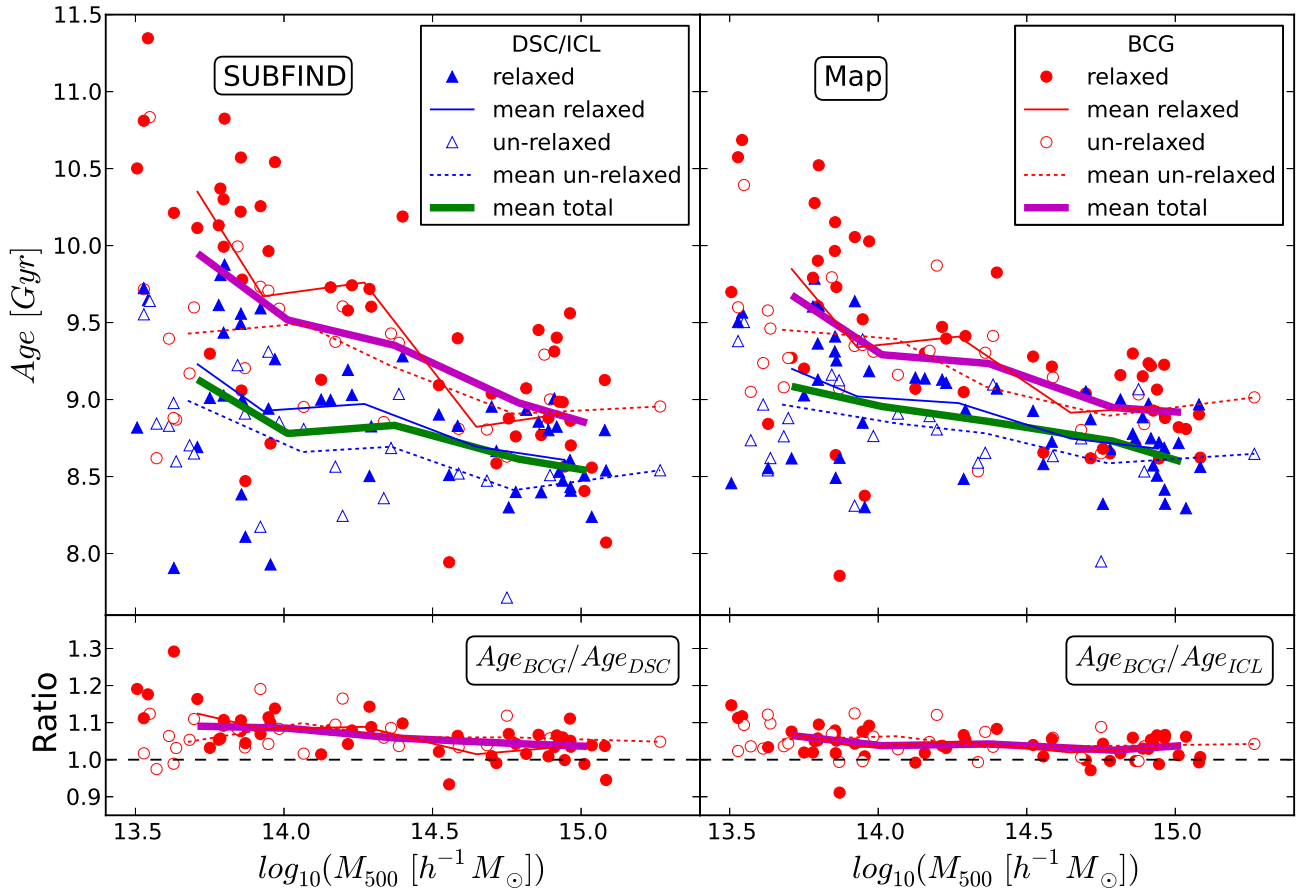

Figure 14. Upper panels: average, mass-weighted age of BCGs and the DSC/ICL (left: SUBFIND; right: MAP). Lower panels: ratios of ages of the BCG and the DSC/ICL. The symbols are the same as in Fig. 12.

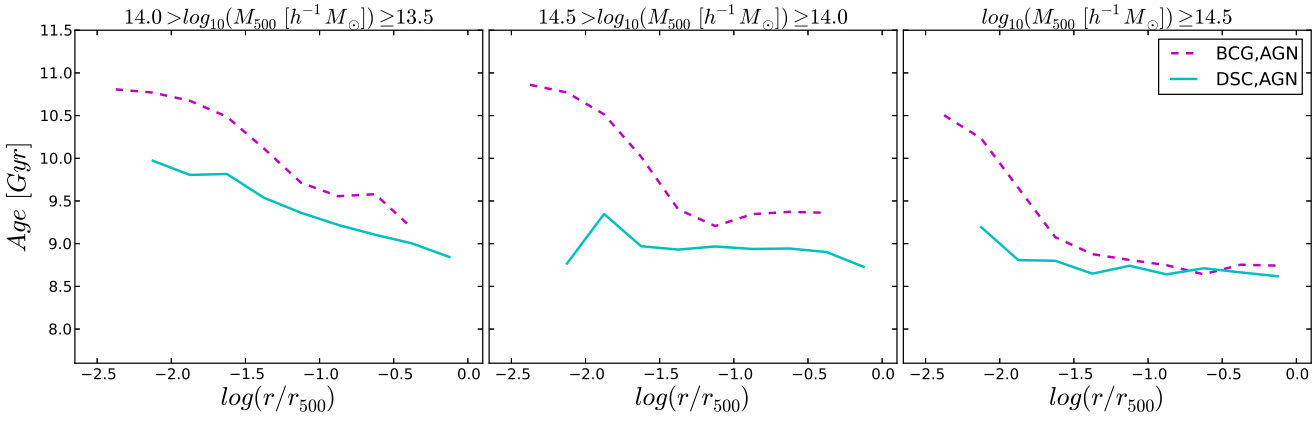

Figure 15. Average age profiles of BCGs (purple dashed line) and the DSC (solid cyan line) stars as found by dynamical method, as a function of radius (normalized to r_{500}), in three different mass-limited subsamples as reported in the label above the panels.

a large object-by-object scatter and a weak trend with mass in the CSF case.

- The velocity dispersions σ of both BCGs and the DSC show a tight scaling with the total cluster mass, $\sigma \propto M_{200}^{\alpha}$, with $\alpha \simeq 0.36$. At fixed M_{200} the velocity dispersion of the DSC is larger than that of the BCG by about a factor of 2, consistent with the fact that the DSC is associated with the broader Maxwellian velocity distribution. These results are consistent with observational evidence for a larger value of the velocity dispersion of the DSC with respect to that of the BCG (e.g. Melnick et al. 2012).
- The DSC and ICL components show similar ages and

metallicities, but both lower than the BCG ones. Age and metallicity profiles of stars identified as belonging to the BCG or the DSC by the dynamical method significantly differ in the central parts, dominated by the BCG. The BCG stars lying in the central regions are older and more metal rich than the DSC stars.

The analysis of our simulations shows in general that the DSC in galaxy clusters represents a distinct population with respect to the component associated with the BCG. These two components not only have different kinematics, thereby hinting to a different dynamical origin, but are also characterized by different ages and metallicity. These results are generally in line with observational evidence, thus demonstrating that simulations are able to capture the basic phenomena leading to the generation of the intra-cluster stellar populations. Still, a quantitative comparison with observational data demonstrates the existence of a tension with predictions from simulations. First of all, even with the inclusion of AGN feedback, simulations still produce BCGs that tend to be more massive than the observed ones (see also Ragone-Figueroa et al. 2013, and references therein). As a consequence, identifying ICL in simulations based on the same surface brightness limit adopted in observational data can not lead to an identical comparison between real and simulated clusters. On the other hand, observational measurements of the stellar mass of the BCG are also prone to systematic uncertainties, especially if they are based on photometric data, combined with a suitable value for the stellar mass-to-light ratio, usually assumed to be constant.

There is little doubt that fully exploiting the potential of the diffuse intra-cluster stars as tracers of the past assembly and star-formation histories in galaxy clusters requires a leap forward in the observational characterization of this elusive component. Furthermore, it also requires simulations to include reliable descriptions of the key astrophysical processes which regulate the evolution of this galaxy population.

ACKNOWLEDGEMENTS

The authors would like to thank Mario Nonino for useful discussions. All the figures in this paper are plotted using the python matplotlib package (Hunter 2007). Simulations have been carried out at the CINECA supercomputing Centre in Bologna, with CPU time assigned through ISCRA proposals and through an agreement with the University of Trieste. WC and MK acknowledge a fellowship from the European Commission's Framework Programme 7, through the Marie Curie Initial Training Network CosmoComp (PITN-GA-2009-238356). PM and SB acknowledge support from FRA2009 grant from the University of Trieste. GDL acknowledges financial support from the European Research Council under the European Community's Seventh Framework Programme (FP7/2007-2013)/ERC grant agreement n. 202781. This work is partially supported by the PRIN/MIUR-2009 grant "Tracing the growth of cosmic structures", by the PRIN-INAF 2010 grant "Towards an italian network for computational cosmology" and by the PD51-INFN grant. KD acknowledges the support by the DFG Cluster of Excellence "Origin and Structure of the Universe".

REFERENCES

Aguerri J. A. L., Gerhard O. E., Arnaboldi M., Napolitano N. R., Castro-Rodriguez N., Freeman K. C., 2005, The Astronomical Journal, 129, 2585
Arnaboldi M., Gerhard O., 2010, Highlights of Astronomy, 15, 97
Arnaboldi M., Ventimiglia G., Iodice E., Gerhard O., Coccato L., 2012, A&A, 545, A37
Barai P., Brito W., Martel H., 2009, Journal of Astrophysics and Astronomy, 30, 1
Bernstein G. M., Nichol R. C., Tyson J. A., Ulmer M. P., Wittman D., 1995, AJ, 110, 1507
Bonafede A., Dolag K., Stasyszyn F., Murante G., Borgani S., 2011, Monthly Notices of the Royal Astronomical Society, 418, 2234
Bruzual G., Charlot S., 2003, MNRAS, 344, 1000
Burke C., Collins C. A., Stott J. P., Hilton M., 2012, Monthly Notices of the Royal Astronomical Society, 425, 2058
Chabrier G., 2003, The Publications of the Astronomical Society of the Pacific, 115, 763
Ciardullo R., Sigurdsson S., Feldmeier J. J., Jacoby G. H., 2005, ApJ, 629, 499
Coccato L., Gerhard O., Arnaboldi M., Ventimiglia G., 2011, A&A, 533, A138
Conroy C., Dutton A. A., Graves G. J., Mendel J. T., van Dokkum P. G., 2013, ApJ, 776, L26
Conroy C., van Dokkum P. G., 2012, ApJ, 760, 71
Conroy C., Wechsler R. H., Kravtsov A. V., 2007, The Astrophysical Journal, 668, 826
Contini E., et al. 2013, submitted to MNRAS
Cui W., Springel V., Yang X., De Lucia G., Borgani S., 2011, Monthly Notices of the Royal Astronomical Society, 416, 2997
De Lucia G., Borgani S., 2012, MNRAS, 426, L61
Doherty M., Arnaboldi M., Das P., Gerhard O., Aguerri J. A. L., Ciardullo R., Feldmeier J. J., Freeman K. C., Jacoby G. H., Murante G., 2009, A&A, 502, 771
Dolag K., Borgani S., Murante G., Springel V., 2009, MNRAS, 399, 497
Dolag K., Murante G., Borgani S., 2010, MNRAS, 405, 1544
Durrell P. R., Ciardullo R., Feldmeier J. J., Jacoby G. H., Sigurdsson S., 2002, The Astrophysical Journal, 570, 119
Fabjan D., Borgani S., Rasia E., Bonafede A., Dolag K., Murante G., Tornatore L., 2011, Monthly Notices of the Royal Astronomical Society, 416, 801
Fabjan D., Borgani S., Tornatore L., Saro A., Murante G., Dolag K., 2010, Monthly Notices of the Royal Astronomical Society, 401, 1670
Feldmeier J. J., Ciardullo R., Jacoby G. H., Durrell P. R., 2004, ApJ, 615, 196
Feldmeier J. J., Mihos J. C., Morrison H. L., Rodney S. A., Harding P., 2002, ApJ, 575, 779
Ferland G. J., Korista K. T., Verner D. A., Ferguson J. W., Kingdon J. B., Verner E. M., 1998, PASP, 110, 761
Gerhard O., Arnaboldi M., Freeman K. C., Okamura S., Kashikawa N., Yasuda N., 2007, A&A, 468, 815
Gonzalez A. H., Zabludoff A. I., Zaritsky D., 2005, The Astrophysical Journal, 618, 195
Gonzalez A. H., Zaritsky D., Zabludoff A. I., 2007, ApJ,

666, 147
Gregg M. D., West M. J., 1998, Nature, 396, 549
Guennou L., Adami C., Da Rocha C., Durret F., Ulmer M. P., Allam S., Basa S., Benoist C., Biviano A., Clowe D., Gavazzi R., Halliday C., Ilbert O., Johnston D., Just D., Kron R., et al. 2012, A&A, 537, A64
Guo Q., White S., Boylan-Kolchin M., De Lucia G., Kauffmann G., Lemson G., Li C., Springel V., Weinmann S., 2011, Monthly Notices of the Royal Astronomical Society, 413, 101
Haardt F., Madau P., 2001, in Neumann D. M., Tran J. T. V., eds, Clusters of Galaxies and the High Redshift Universe Observed in X-rays Modelling the UV/X-ray cosmic background with CUBA
Henriques B. M., Bertone S., Thomas P. A., 2008, MNRAS, 383, 1649
Holmberg E., 1958, Meddelanden fran Lunds Astronomiska Observatorium Serie II, 136, 1
Hunter J. D., 2007, Computing In Science & Engineering, 9, 90
Kang X., van den Bosch F. C., 2008, The Astrophysical Journal, 676, L101
Killedar M., Borgani S., Meneghetti M., Dolag K., Fabjan D., Tornatore L., 2012, MNRAS, 427, 533
Krick J. E., Bernstein R. A., 2007, Monthly Notices of the Royal Astronomical Society, 134, 466
Lin Y.-T., Mohr J. J., 2004, The Astrophysical Journal, 617, 879
Liu L., Yang X., Mo H. J., van den Bosch F. C., Springel V., 2010, The Astrophysical Journal, 712, 734
Lo Faro B., Monaco P., Vanzella E., Fontanot F., Silva L., Cristiani S., 2009, MNRAS, 399, 827
Martel H., Barai P., Brito W., 2012, The Astrophysical Journal, 757, 48
Melnick J., Giraud E., Toledo I., Selman F., Quintana H., 2012, MNRAS, 427, 850
Mihos J. C., Harding P., Feldmeier J., Morrison H., 2005, The Astrophysical Journal, 631, L41
Monaco P., Murante G., Borgani S., Fontanot F., 2006, ApJ, 652, L89
Munari E., Biviano A., Borgani S., Murante G., Fabjan D., 2013, MNRAS, 430, 2638
Murante G., Arnaboldi M., Gerhard O., Borgani S., Cheng L. M., Diaferio A., Dolag K., Moscardini L., Tormen G., Tornatore L., Tozzi P., 2004, The Astrophysical Journal, 607, L83
Murante G., Giovalli M., Gerhard O., Arnaboldi M., Borgani S., Dolag K., 2007, Monthly Notices of the Royal Astronomical Society, 377, 2
Newman A. B., Treu T., Ellis R. S., Sand D. J., Nipoti C., Richard J., Jullo E., 2013, ApJ, 765, 24
Padovani P., Matteucci F., 1993, ApJ, 416, 26
Planelles S., Borgani S., Dolag K., Ettori S., Fabjan D., Murante G., Tornatore L., 2013, MNRAS, 431, 1487
Postman M., Lauer T. R., Donahue M., Graves G., Coe D., Moustakas J., Koekemoer A., Bradley L., Ford H. C., Grillo C., Zitrin A., Lemze D., Broadhurst T., Moustakas L., Ascaso B., Medezinski E., Kelson D., 2012, ApJ, 756, 159
Puchwein E., Springel V., Sijacki D., Dolag K., 2010, Monthly Notices of the Royal Astronomical Society, 406, 936
Purcell C. W., Bullock J. S., Zentner A. R., 2007, The Astrophysical Journal, 666, 20
Ragone-Figueroa C., Granato G. L., Murante G., Borgani S., Cui W., 2013, MNRAS
Rudick C. S., 2010, ProQuest Dissertations And Theses; Thesis (Ph.D.)–Case Western Reserve University, p. 88
Rudick C. S., Mihos J. C., Frey L. H., McBride C. K., 2009, The Astrophysical Journal, 699, 1518
Rudick C. S., Mihos J. C., Harding P., Feldmeier J. J., Janowiecki S., Morrison H. L., 2010, The Astrophysical Journal, 720, 569
Rudick C. S., Mihos J. C., McBride C., 2006, The Astrophysical Journal, 648, 936
Rudick C. S., Mihos J. C., McBride C. K., 2011, The Astrophysical Journal, 732, 48
Salpeter E. E., 1955, Astrophysical Journal, 121, 161
Sand D. J., Graham M. L., Bildfell C., Foley R. J., Pritchet C., Zaritsky D., Hoekstra H., Just D. W., Herbert-Fort S., Sivanandam S., 2011, ApJ, 729, 142
Seigar M. S., Graham A. W., Jerjen H., 2007, MNRAS, 378, 1575
Sijacki D., Springel V., Di Matteo T., Hernquist L., 2007, MNRAS, 380, 877
Somerville R. S., Hopkins P. F., Cox T. J., Robertson B. E., Hernquist L., 2008, MNRAS, 391, 481
Sommer-Larsen J., Romeo A. D., Portinari L., 2005, Monthly Notices of the Royal Astronomical Society, 357, 478
Spiniello C., Trager S., Koopmans L. V. E., Conroy C., 2013, ArXiv e-prints
Springel V., 2005, Monthly Notices of the Royal Astronomical Society, 364, 1105
Springel V., Di Matteo T., Hernquist L., 2005, ApJ, 620, L79
Springel V., Hernquist L., 2003, MNRAS, 339, 289
Springel V., White S. D. M., Tormen G., Kauffmann G., 2001, Monthly Notices of the Royal Astronomical Society, 328, 726
Theuns T., Warren S. J., 1997, MNRAS, 284, L11
Toledo I., Melnick J., Selman F., Quintana H., Giraud E., Zelaya P., 2011, Monthly Notices of the Royal Astronomical Society, 414, 602
Tormen G., Bouchet F. R., White S. D. M., 1997, Monthly Notices of the Royal Astronomical Society, 286, 865
Tornatore L., Borgani S., Dolag K., Matteucci F., 2007, MNRAS, 382, 1050
Trentham N., Mobasher B., 1998, Monthly Notices of the Royal Astronomical Society, 293, 53
Tutukov A. V., Dryomov V. V., Dryomova G. N., 2007, Astronomy Reports, 51, 435
Watson D. F., Berlind A. A., Zentner A. R., 2012, The Astrophysical Journal, 754, 90
Wiersma R. P. C., Schaye J., Smith B. D., 2009, MNRAS, 393, 99
Williams B. F., Ciardullo R., Durrell P. R., Vinciguerra M., Feldmeier J. J., Jacoby G. H., Sigurdsson S., von Hippel T., Ferguson H. C., Tanvir N. R., Arnaboldi M., Gerhard O., Aguerri J. A. L., Freeman K., 2007, ApJ, 656, 756
Willman B., Governato F., Wadsley J., Quinn T., 2004, Monthly Notices of the Royal Astronomical Society, 355, 159
Wurster J., Thacker R. J., 2013, MNRAS, 431, 2513

Yang X., Mo H. J., van den Bosch F. C., 2009, ApJ, 693, 830
Zibetti S., White S. D. M., Schneider D. P., Brinkmann J., 2005, Monthly Notices of the Royal Astronomical Society, 358, 949
Zwicky F., 1951, Publications of the Astronomical Society of the Pacific, 63, 61